Inverse Problems and Imaging
Volume 9, No. 1, 2015, 189–210
doi:10.3934/ipi.2015.9.189

NEAR-FIELD IMAGING OF OBSTACLES

Peijun Li and Yuliang Wang

Department of Mathematics
Purdue University
West Lafayette, IN 47907, USA

(Communicated by Fioralba Cakoni)

Abstract. A novel method is developed for solving the inverse obstacle scattering problem in near-field imaging. The obstacle surface is assumed to be a small and smooth deformation of a circle. Using the transformed field expansion, the direct obstacle scattering problem is reduced to a successive sequence of two-point boundary value problems. Analytical solutions of these problems are derived by a Green's function method. The nonlinear inverse problem is linearized by dropping the higher order terms in the power series expansion. Based on the linear model and analytical solutions, an explicit reconstruction formula is obtained. In addition, a nonlinear correction scheme is devised to improve the results dramatically when the deformation is large. The method requires only a single incident wave at a fixed frequency. Numerical tests show that the method is stable and effective for near-field imaging of obstacles with subwavelength resolution.

1. **Introduction.** Obstacle scattering problems are concerned with how an incident wave is scattered by a bounded impenetrable medium. The direct problem is to determine the wave field from a knowledge of the obstacle, while the inverse problem is to determine the obstacle from the measured wave field. These problems have played a fundamental role in diverse scientific areas such as radar and sonar, geophysical exploration, medical imaging, nondestructive testing [15], and more recently near-field optics [11, 16].

The direct problem has been studied extensively by numerous researchers via either boundary integral equation methods or variational approaches [14]. Computational methods can be classified into two categories for solving the inverse problem: nonlinear optimization based iterative methods and imaging based direct methods. The former are known as quantitative methods and are aimed at recovering unknown functions which represent the obstacles [18, 20, 23, 24]. These methods are computationally more intensive as a sequence of direct and adjoint scattering problems need to be solved at iterations. The latter are called qualitative methods and attempt to visualize the obstacles by highlighting the boundary with designed imaging functions [10, 13, 19, 21, 31, 32]. They are computationally more efficient but are not as accurate as those quantitative methods.

In far-field imaging, data is measured at a distance which is a few wavelength or longer away from the targets, which imposes a limit on the sharpness of details

2010 *Mathematics Subject Classification.* Primary: 58F15, 58F17; Secondary: 53C35.
Key words and phrases. Near-field imaging, inverse obstacle scattering, transformed field expansion.
This research was supported in part by the NSF grant DMS-1151308.

on the reconstructions. This resolution limit is about half of the wavelength and is referred to as the Rayleigh criterion or the diffraction limit [17]. Near-field imaging and is an effective approach to break the diffraction limit [16]. It has led to emerging applications in modern science and technology, such as nanotechnology, biology, information storage, and surface chemistry. Using near-field imaging, we intend to develop an effective mathematical model and an efficient computational method for solving the inverse obstacle scattering problem.

As a model problem, we consider the scattering of a time-harmonic acoustic wave by a sound soft obstacle in two dimensions. The obstacle is assumed to be a small and smooth deformation of a disk. Specifically, an incoming cylindrical wave is incident upon the obstacle from infinity and generates a scattered field. The direct problem is to determine the total field in the exterior space given the obstacle. We are mainly interested in the inverse problem: to reconstruct the obstacle given the measured field at a fixed distance away from the obstacle. The inverse problem is challenging because of the intrinsic nature of nonlinearity and ill-posedness.

In this paper, a boundary value problem (BVP) is formulated for the total field in a bounded domain by using a transparent boundary condition. Based on the transformed field expansion, the total field is expanded as a power series of deformation parameter; the coefficient functions satisfy a successive sequence of BVPs in an annular domain. By using the Fourier series expansion, each of the BVPs is further reduced into a two-point BVP and solved analytically by the Green's function method. The nonlinear relation between the obstacle and the measured field is approximated by a linear equation by dropping the higher order terms in the power series expansion. An explicit reconstruction formula is finally obtained by using the derived analytical expressions for the zeroth and first order terms. The spectral cut-off regularization method is adopted to obtain stable reconstruction in the numerical computation. In addition, a nonlinear correction method is developed to improve the results for larger deformations. To avoid the so-called "inverse crime", the measurement data is simulated by solving the direct problem by using a derived integral equation method rather than the transformed field expansion method. Our method requires only a single incident wave at a fixed frequency. Numerical experiments show that the method is stable and effective for reconstructing the obstacles with subwavelength resolution. Transformed field expansion and related boundary perturbation methods have been applied for solving the direct obstacle scattering problem [30], the direct rough surface scattering problem [25, 28, 29], and the direct diffraction grating problem [9, 26]. A boundary perturbation method is used to solve an inverse scattering problem with a periodic layered medium [27]. Interested readers are referred to [2, 3, 7, 8] for other related inverse problems in near-field imaging.

This paper is an extension of our recent work on near-field imaging of infinite and periodic rough surfaces [4, 5, 1, 12]. Due to the notable change in the problem geometry, this work differs in several important aspects. First, the incident field is a cylindrical wave rather than a plane wave. The major motivation for this consideration is to make the reconstruction formula as simple as possible. Besides, it is a natural choice since the fundamental solution for the direct obstacle scattering problem is composed of cylindrical functions instead of complex exponential functions. This observation gives rise to the second difference: the derivation for the analytical solutions to the two-point BVPs and the reconstruction formula become

more complicated. Though the reconstruction formula is less explicit and the ill-posed nature is not immediately available, the numerical results indicate that the present problem has a similar nature of ill-posedness of those previous work.

The paper is organized as follows. The model problem is introduced in Section 2. In Section 3, an analytical solution is obtained from the transformed field and Fourier expansions. An explicit reconstruction formula and a nonlinear correction scheme are presented in Section 4. Numerical results are presented and discussed in Section 5. We conclude the paper with remarks and direction for future work in Section 6.

2. **Model problem.** As seen in Figure 1, the obstacle is assumed to be a small and smooth deformation of a disk in $\mathbb{R}^2$, so that it can be defined by the domain

$$\Omega = \{(r,\theta) : 0 < r < a + f(\theta),\ 0 \le \theta < 2\pi\}.$$

Here $a > 0$ is a constant and $f \in C^2(\mathbb{R})$ is a 2π-periodic function which can be written as

$$f(\theta) = \varepsilon g(\theta), \tag{1}$$

where $\varepsilon > 0$ is a small deformation parameter and $g \in C^2(\mathbb{R})$ is a 2π-periodic function describing the profile of the obstacle. To reduce the problem into a bounded domain, we consider

$$D = \{(r,\theta) : a + f(\theta) < r < b,\ 0 \le \theta < 2\pi\},$$

where $b > a + ||f(\theta)||_\infty$ is a constant and $r = b$ is the boundary where the data is taken for the inverse problem.

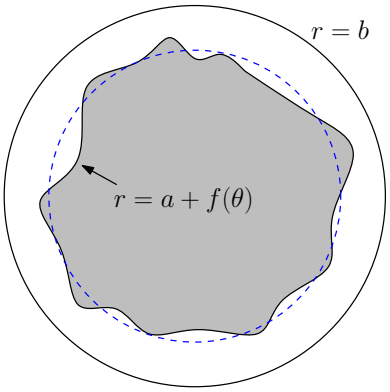

FIGURE 1. Geometry of the model problem.

Let the exterior domain $\mathbb{R}^2 \setminus \bar{\Omega}$ be filled with a homogeneous medium with a constant wavenumber κ. An incoming cylindrical wave

$$u^{\text{inc}}(r,\theta) = H_0^{(2)}(\kappa r) \tag{2}$$

is incident upon the obstacle from outside, where $H_0^{(2)}$ is the zeroth order Hankel function of the second kind.

Remark 1. As we shall see later, this particular choice of the incident field simplifies the mathematical model and yields a more explicit reconstruction formula. The calculations are more tedious for the reconstruction formula which may not benefit

a clear presentation of the method, even though it is a common choice using the plane wave to illuminate the obstacle.

The total field u satisfies the Helmholtz equation

$$\left(\Delta + \kappa^2\right) u(r,\theta) = 0 \quad \text{in } D, \tag{3}$$

where the Laplace operator Δ is given in the polar coordinate by

$$\Delta = \partial_{rr} + \frac{1}{r}\partial_r + \frac{1}{r^2}\partial_{\theta\theta}.$$

For a sound soft obstacle, u vanishes on the inner boundary of D:

$$u(r,\theta) = 0 \quad \text{on } r = a + f(\theta). \tag{4}$$

The total field u consists of the incident field u^{inc} and the scattered field u^{sca}, i.e., $u = u^{\text{inc}} + u^{\text{sca}}$. Evidently, we have

$$\left(\Delta + \kappa^2\right) u^{\text{sca}}(r,\theta) = 0 \quad \text{in } D. \tag{5}$$

In addition, u^{sca} is required to satisfy the Sommerfeld radiation condition

$$(\partial_r - \mathrm{i}\kappa) u^{\text{sca}}(r,\theta) = o(r^{-1/2}) \quad \text{as } r \to \infty. \tag{6}$$

Using separation of variables and periodicity of $u^{\text{sca}}(r,\theta)$ in θ, we obtain that the general solution of (5) and (6) can be written as the Fourier series expansion

$$u^{\text{sca}}(r,\theta) = \sum_{n\in\mathbb{Z}} a_n H_n^{(1)}(\kappa r) e^{\mathrm{i}n\theta}, \ r \geq b, \tag{7}$$

where $H_n^{(1)}$ is the n-th Hankel function of the first kind. Taking partial derivative with respect to r on both sides of (7) yields

$$\partial_r u^{\text{sca}}(r,\theta) = \sum_{n\in\mathbb{Z}} \kappa a_n H_n^{(1)'}(\kappa r) e^{\mathrm{i}n\theta}, \quad r \geq b. \tag{8}$$

Evaluating (7) and (8) at $r = b$ and comparing the Fourier coefficients, we obtain the transparent boundary condition for u^{sca}:

$$\left(\partial_r - T\right) u^{\text{sca}}(r,\theta) = 0 \quad \text{on } r = b. \tag{9}$$

For any 2π-periodic function ϕ, the boundary operator T is defined by

$$T(\phi) = \sum_{n\in\mathbb{Z}} \frac{\kappa H_n^{(1)'}(\kappa b)}{H_n^{(1)}(\kappa b)} \phi_n e^{\mathrm{i}n\theta}.$$

Applying $\partial_r - T$ to the incident field in (2) yields

$$\left(\partial_r - T\right) u^{\text{inc}}(b,\theta) = \psi = -\frac{4\mathrm{i}}{\pi b H_0^{(1)}(\kappa b)}, \tag{10}$$

where we have used the formula for the Wronskian of Hankel functions [22]:

$$H_0^{(1)}(z) H_0^{(2)'}(z) - H_0^{(1)'}(z) H_0^{(2)}(z) = -\frac{4\mathrm{i}}{\pi z}.$$

Finally, adding (9) to (10) yields the transparent boundary condition for u:

$$\left(\partial_r - T\right) u(r,\theta) = \psi \quad \text{on } r = b. \tag{11}$$

The direct problem is to solve the BVP of $u(r,\theta)$ by (3), (4) and (11) given the obstacle deformation function $f(\theta)$. The inverse problem is to reconstruct $f(\theta)$ from the measured field $u_\delta(b,\theta)$, where δ is the noise level. To obtain subwavelength

resolution in a stable manner, the measurement distance $h = b-a$ needs to be much smaller than the wavelength $\lambda = \kappa/2\pi$.

Remark 2. Although this particular modality, i.e., to measure the field close to and all around the obstacle, may not be done in experiments as far as we know, similar configurations have been realized, such as in the photon scanning tunneling microscopy [16], to measure the field closely in a constant height above a surface.

3. **Transformed field expansion.** In this section we adopt the transformed field expansion to obtain an analytical solution for the direct problem.

Consider the change of variables:

$$\tilde{r} = \frac{hr - bf(\theta)}{h - f(\theta)}, \quad \tilde{\theta} = \theta,$$

which transforms D to an annulus with inner radius a and outer radius b. Applying the chain rule, we may verify that

$$\begin{aligned}
\partial_r =& \partial_{\tilde{r}} \frac{\partial_{\tilde{r}}}{\partial_r} + \partial_{\tilde{\theta}} \frac{\partial_{\tilde{\theta}}}{\partial_r} = \frac{h}{h-f} \partial_{\tilde{r}}, \\
\partial_\theta =& \partial_{\tilde{r}} \frac{\partial_{\tilde{r}}}{\partial_\theta} + \partial_{\tilde{\theta}} \frac{\partial_{\tilde{\theta}}}{\partial_\theta} = \frac{f'}{h-f}(\tilde{r}-b)\partial_{\tilde{r}} + \partial_{\tilde{\theta}}, \\
\partial_{rr} =& \left(\frac{h}{h-f}\right)^2 \partial_{\tilde{r}\tilde{r}}, \\
\partial_{\theta\theta} =& \left(\frac{f'}{h-f}\right)^2 (\tilde{r}-b)^2 \partial_{\tilde{r}\tilde{r}} + \frac{f''(h-f)+2(f')^2}{(h-f)^2}(\tilde{r}-b)\partial_{\tilde{r}} \\
&+ \frac{2f'}{h-f}(\tilde{r}-b)\partial_{\tilde{r}\tilde{\theta}} + \partial_{\tilde{\theta}\tilde{\theta}}.
\end{aligned}$$

Letting $w(\tilde{r}, \tilde{\theta}) = u(r, \theta)$ and substituting the above relations into the Helmholtz equation (3), we obtain, after dropping the tilde for simplicity of notation, that

$$\left(c_1 \partial_{rr} + c_2 \frac{1}{r}\partial_r + c_3 \frac{1}{r}\partial_{r\theta} + c_4 \frac{1}{r^2}\partial_{\theta\theta} + c_5 \frac{1}{r^2}\kappa^2\right) w(r,\theta) = 0, \quad a < r < b, \tag{12}$$

where

$$\begin{aligned}
c_1 =& h^2 - 2h\left(1-\frac{b}{r}\right) f + \frac{1}{r^2} f^2 + \left(1-\frac{b}{r}\right)^2 (f')^2, \\
c_2 =& h^2 - \left(2-\frac{b}{r}\right) hf + \left(1-\frac{b}{r}\right) hf'' \\
&+ \left(1-\frac{b}{r}\right) f^2 + 2\left(1-\frac{b}{r}\right)(f')^2 - \left(1-\frac{b}{r}\right) ff'', \\
c_3 =& 2\left(1-\frac{b}{r}\right)(hf' - ff'), \\
c_4 =& h^2 - 2hf + f^2,
\end{aligned}$$

$$c_5 = h^2 - 2h\left(2 - \frac{b}{r}\right) f + \left[6 - 6\left(\frac{b}{r}\right) + \left(\frac{b}{r}\right)^2\right] f^2 - \frac{2}{h}\left(1 - \frac{b}{r}\right)\left(2 - \frac{b}{r}\right) f^3 + \frac{1}{h^2}\left(1 - \frac{b}{r}\right)^2 f^4.$$

The Dirichlet boundary condition (4) becomes

$$w(r,\theta) = 0 \quad \text{on } r = a,$$

and the transparent boundary condition (11) reduces to

$$\partial_r w(r,\theta) = \left(1 - \frac{f}{h}\right)[Tw(r,\theta) + \psi] \quad \text{on } r = b. \tag{13}$$

Hence the original BVP for the total field u is transformed to a BVP for w given by (12)–(13).

3.1. **Power series expansion.** Due to the small perturbation assumption (36), we may consider a formal expansion of $w(r,\theta)$ as a power series in ε:

$$w(r,\theta) = \sum_{m=0}^{\infty} w_m(r,\theta)\varepsilon^m. \tag{14}$$

Substituting $f = \varepsilon g$ into the defining equations for c_j and collecting terms according to the power of ε, we obtain

$$\begin{aligned}
c_1 &= h^2 - 2h\left(1 - \frac{b}{r}\right) g\varepsilon + \left[g^2 + \left(1 - \frac{b}{r}\right)^2 (g')^2\right]\varepsilon^2,\\
c_2 &= h^2 + h\left[\left(1 - 2\frac{b}{r}\right) g + \left(1 - \frac{b}{r}\right) g''\right]\varepsilon\\
&\quad + \left(1 - \frac{b}{r}\right)\left[g^2 + 2(g')^2 - gg''\right]\varepsilon^2,\\
c_3 &= 2h\left(1 - \frac{b}{r}\right) g'\varepsilon - 2\left(1 - \frac{b}{r}\right) gg'\varepsilon^2,\\
c_4 &= h^2 - 2hg\varepsilon + g^2\varepsilon^2,\\
c_5 &= h^2 - 2h\left(2 - \frac{b}{r}\right) g\varepsilon + \left[6 - 6\left(\frac{b}{r}\right) + \left(\frac{b}{r}\right)^2\right] g^2\varepsilon^2\\
&\quad - \frac{2}{h}\left(1 - \frac{b}{r}\right)\left(2 - \frac{b}{r}\right) g^3\varepsilon^3 + \frac{1}{h^2}\left(1 - \frac{b}{r}\right)^2 g^4\varepsilon^4.
\end{aligned}$$

Substituting these expressions and (14) into (12) yields a successive sequence of equations for w_m:

$$\left(\Delta + \kappa^2\right) w_m = v_m, \tag{15}$$

where

$$
\begin{aligned}
v_m =& \frac{1}{h}\left\{2\left(1-\frac{b}{r}\right)g\partial_{rr}+\left[\left(2-\frac{b}{r}\right)g-\left(1-\frac{b}{r}\right)g''\right]\frac{1}{r}\partial_r\right.\\
&\left.-2\left(1-\frac{b}{r}\right)g'\frac{1}{r}\partial_{r\theta}+2g\frac{1}{r^2}\partial_{\theta\theta}+2\left(2-\frac{b}{r}\right)\kappa^2 g\right\}w_{m-1}\\
&+\frac{1}{h^2}\left\{\left[-g^2-\left(1-\frac{b}{r}\right)^2(g')^2\right]\partial_{rr}-\left(1-\frac{b}{r}\right)\left[g^2+2(g')^2-gg''\right]\frac{1}{r}\partial_r\right.\\
&\left.+2\left(1-\frac{b}{r}\right)gg'\frac{1}{r}\partial_{r\theta}-g^2\frac{1}{r^2}\partial_{\theta\theta}-\left[6-6\left(\frac{b}{r}\right)+\left(\frac{b}{r}\right)^2\right]g^2\kappa^2\right\}w_{m-2}\\
&+\frac{1}{h^3}\left[2\left(1-\frac{b}{r}\right)\left(2-\frac{b}{r}\right)g^3\kappa^2\right]w_{m-3}\\
&+\frac{1}{h^4}\left[-\left(1-\frac{b}{r}\right)^2 g^4\kappa^2\right]w_{m-4}. \qquad (16)
\end{aligned}
$$

Similarly we obtain the Dirichlet boundary condition

$$w_m(r,\theta)=0 \quad \text{on } r=a, \qquad (17)$$

and the transparent boundary conditions

$$(\partial_r - T)w_m(r,\theta)=\psi_m(\theta) \quad \text{on } r=b, \qquad (18)$$

where

$$\psi_0=\psi,\ \psi_1=-\frac{g}{h}\left(Tw_0(b,\theta)+\psi\right),\ \psi_m=-\frac{g}{h}Tw_{m-1}(b,\theta). \qquad (19)$$

It is understood that $w_m = 0$ for $m < 0$ in all the above recurrence relations. Thus all the terms w_m in the power series (14) can be obtained by solving the BVPs (15), (17), and (18) recursively starting from $m = 0$.

3.2. **Fourier series expansion.** To reduce the problems further and derive analytical solutions, we consider each BVP for w_m in the frequency domain. Since $w_m(r,\theta), v_m(r,\theta)$, and $\psi_m(\theta)$ are 2π-periodic functions in θ, we have the following Fourier series expansions:

$$
\begin{aligned}
w_m(r,\theta)&=\sum_{n\in\mathbb{Z}} w_m^{(n)}(r)e^{in\theta},\\
v_m(r,\theta)&=\sum_{n\in\mathbb{Z}} v_m^{(n)}(r)e^{in\theta},\\
\psi_m(\theta)&=\sum_{n\in\mathbb{Z}} \psi_m^{(n)}e^{in\theta}.
\end{aligned}
$$

Substituting the expansions into (15), (17), (18) and applying the definition of T, we obtain the two-point BVP for $w_m^{(n)}$:

$$\left[\frac{\mathrm{d}^2}{\mathrm{d}r^2}+\frac{1}{r}\frac{\mathrm{d}}{\mathrm{d}r}+\left(\kappa^2-\frac{n^2}{r^2}\right)\right]w_m^{(n)}(r)=v_m^{(n)}(r), \quad \text{in } (a,b) \qquad (20)$$

$$w_m^{(n)}(a)=0, \qquad (21)$$

$$\left[\frac{\mathrm{d}}{\mathrm{d}r} - \frac{\kappa H_n^{(1)'}(\kappa b)}{H_n^{(1)}(\kappa b)}\right] w_m^{(n)}(b) = \psi_m^{(n)}. \tag{22}$$

For simplicity, we normalize all variables with respect to the wavenumber κ through the change of variables:

$$\hat{r} = \kappa r, \quad \hat{a} = \kappa a, \quad \hat{b} = \kappa b, \tag{23}$$

$$\hat{w}_m^{(n)}(\hat{r}) = w_m^{(n)}(r), \quad \hat{v}_m^{(n)}(\hat{r}) = \kappa^{-2} v_m^{(n)}(r), \quad \hat{\psi}_m^{(n)} = \kappa^{-1}\psi_m^{(n)}. \tag{24}$$

Substituting (23) and (24) into (20)–(22) yields

$$\left[\frac{\mathrm{d}^2}{\mathrm{d}\hat{r}^2} + \frac{1}{\hat{r}}\frac{\mathrm{d}}{\mathrm{d}\hat{r}} + \left(1 - \frac{n^2}{\hat{r}^2}\right)\right] \hat{w}_m^{(n)}(\hat{r}) = \hat{v}_m^{(n)}(\hat{r}), \quad \text{in } (\hat{a}, \hat{b}) \tag{25}$$

$$\hat{w}_m^{(n)}(\hat{a}) = 0, \tag{26}$$

$$\left[\frac{\mathrm{d}}{\mathrm{d}\hat{r}} - \frac{H_n^{(1)'}(\hat{b})}{H_n^{(1)}(\hat{b})}\right] \hat{w}_m^{(n)}(\hat{b}) = \hat{\psi}_m^{(n)}. \tag{27}$$

Using the analytical solution (B.9) in Appendix B, we have

$$\hat{w}_m^{(n)}(\hat{r}) = G_n(\hat{r}, \hat{b})\hat{\psi}_m^{(n)} - \int_{\hat{a}}^{\hat{b}} G_n(\hat{r}, \hat{s})\hat{v}_m^{(n)}(\hat{s})\mathrm{d}\hat{s}, \tag{28}$$

where

$$G_n(\hat{r}, \hat{s}) = \frac{\mathrm{i}\pi\hat{s}}{4}\begin{cases} E_n(\hat{r})H_n^{(1)}(\hat{s}), & \hat{r} < \hat{s}, \\ E_n(\hat{s})H_n^{(1)}(\hat{r}), & \hat{r} > \hat{s}, \end{cases} \tag{29}$$

and

$$E_n(z) = H_n^{(2)}(z) - \frac{H_n^{(2)}(a)}{H_n^{(1)}(a)} H_n^{(1)}(z) \tag{30}$$

3.3. **Explicit solutions.** Based on the analytical solutions (28), we may derive more explicit forms for the zeroth order term $\hat{w}_0$ and the first order term $\hat{w}_1$.

It follows from (16) and (19) that

$$v_0 = 0, \quad \psi_0 = \psi.$$

Taking Fourier coefficients and using the change of variables (24), we have

$$\hat{v}_0^{(n)} = 0, \quad \hat{\psi}_0^{(n)} = \kappa^{-1}\psi\delta_{0,n},$$

where $\delta_{0,n}$ is the Kronecker delta function. Substituting the above quantities into (28) and using (29) yields

$$\hat{w}_0^{(n)} = E_0(\hat{r})\delta_{0,n},$$

which gives

$$\hat{w}_0(\hat{r}) = E_0(\hat{r}). \tag{31}$$

Remark 3. It is interesting to observe that $u(r, \theta) = \hat{w}_0(\hat{r})$ is just the total field when the obstacle is a disk with radius a, which can be easily verified by solving the BVP for the corresponding direct scattering problem.

After $\hat{w}_0$ is obtained, we may find $\hat{w}_1$ by using the recurrence relation. Applying (16) at $m = 1$ yields

$$v_1(r,\theta) = \frac{1}{h}\left\{2\left(1-\frac{b}{r}\right)g\partial_{rr} + \left[\left(2-\frac{b}{r}\right)g - \left(1-\frac{b}{r}\right)g''\right]\frac{1}{r}\partial_r \right.$$
$$\left. -2\left(1-\frac{b}{r}\right)g'\frac{1}{r}\partial_{r\theta} + 2g\frac{1}{r^2}\partial_{\theta\theta} + 2\left(2-\frac{b}{r}\right)\kappa^2 g\right\} w_0(r,\theta).$$

Since w_0 is independent of the variable θ and $(\Delta+\kappa^2)w_0 = 0$, the above quantity can be reduced to

$$\begin{aligned} v_1(r,\theta) =& \frac{1}{h}\left\{2\left(1-\frac{b}{r}\right)g\partial_{rr} + \left[\left(2-\frac{b}{r}\right)g - \left(1-\frac{b}{r}\right)g''\right]\frac{1}{r}\partial_r \right. \\ & \left. +2\left(2-\frac{b}{r}\right)\kappa^2 g\right\} w_0(r) \\ =& \frac{2g}{h}\left(1-\frac{b}{r}\right)(\Delta+\kappa^2)w_0(r) + \frac{1}{h}\left\{\left[\frac{b}{r}g - \left(1-\frac{b}{r}\right)g''\right]\frac{1}{r}\partial_r + 2\kappa^2 g\right\} w_0(r) \\ =& \frac{1}{h}\left\{\left[\frac{b}{r}g - \left(1-\frac{b}{r}\right)g''\right]\frac{1}{r}\partial_r + 2\kappa^2 g\right\} w_0(r). \end{aligned}$$

Taking Fourier coefficients in θ and using the change of variables (23) and (24), we obtain

$$\hat{v}_1^{(n)}(\hat{r}) = \frac{1}{h}\left\{\left[n^2 + \frac{\hat{b}(1-n^2)}{\hat{r}}\right]\frac{1}{\hat{r}}\partial_{\hat{r}} + 2\right\} E_0(\hat{r})g^{(n)}. \tag{32}$$

Similarly, it follows from (19) that

$$\hat{\psi}_1^{(n)} = \frac{1}{hH_0^{(1)}(\hat{b})}\left[\frac{4\mathrm{i}}{\pi\hat{b}} - E_0(\hat{b})\left(H_0^{(1)}\right)'(\hat{b})\right] g^{(n)}. \tag{33}$$

Substituting (32), (33), into (28) and evaluating at $\hat{r} = \hat{b}$ yield

$$\hat{w}_1^{(n)}(\hat{b}) = C_n g^{(n)}, \tag{34}$$

where

$$C_n = \frac{\mathrm{i}\pi}{4h}H_n^{(1)}(\hat{b})(M_1 - M_2 - M_3), \tag{35}$$

and

$$M_1 = \frac{\hat{b}E_n(\hat{b})}{H_0^{(1)}(\hat{b})}\left[\frac{4\mathrm{i}}{\pi\hat{b}} - E_0(\hat{b})H_0^{(1)'}(\hat{b})\right], \tag{36}$$

$$M_2 = \int_{\hat{a}}^{\hat{b}}\left[n^2 + \frac{\hat{b}(1-n^2)}{\hat{s}}\right]E_n(\hat{s})E_0'(\hat{s})d\hat{s}, \tag{37}$$

$$M_3 = \int_{\hat{a}}^{\hat{b}} 2sE_n(\hat{s})E_0(\hat{s})d\hat{s}. \tag{38}$$

Remark 4. In the work for inverse surface scattering problems [4, 5, 1, 12], we were able to obtain much simpler forms for the scaling factor C_n by evaluating the involved integrals analytically. In this paper we resort to numerical integrations to compute C_n since no futher simplication is possbile.

4. Reconstruction formula.

Based on the transformed field expansion, we are ready to present the explicit reconstruction formula for the linearized inverse problem and the nonlinear correction scheme to improve the results.

4.1. Linearization.

The noisy data is assumed to take the form

$$u_\delta(b,\theta) = u(b,\theta) + \mathcal{O}(\delta),$$

where $u(b,\theta)$ denotes the noise-free data and δ indicates the noise level. Since $w(b,\theta) = u(b,\theta)$, the measurement data may also be rewritten as

$$w_\delta(b,\theta) = w(b,\theta) + \mathcal{O}(\delta). \tag{39}$$

Truncating the power series expansion (14) at $m = 1$ and evaluating at $r = b$, we obtain

$$w(b,\theta) = w_0(b,\theta) + \varepsilon w_1(b,\theta) + \mathcal{O}(\varepsilon^2), \tag{40}$$

where $w_0(b,\theta) = \hat{w}_0(\hat{b})$ is given explicitly by (31) and thus is independent on f. Substituting (40) into (39) and taking Fourier coefficients in θ yields

$$\varepsilon w_1^{(n)}(b) = w_\delta^{(n)}(b) - w_0^{(n)}(b) + \mathcal{O}(\delta) + \mathcal{O}(\varepsilon^2), \tag{41}$$

Multiplying (34) by ε and noticing that $\hat{w}_1^{(n)}(\hat{b}) = w_1^{(n)}(b)$, $f^{(n)} = \varepsilon g^{(n)}$, we obtain

$$\varepsilon w_1^{(n)}(b) = C_n f^{(n)}, \tag{42}$$

where C_n is given by (35). It follows from (41) and (42) that

$$f^{(n)} = S_n[w_\delta^{(n)}(b) - w_0^{(n)}(b) + \mathcal{O}(\delta) + \mathcal{O}(\varepsilon^2)], \tag{43}$$

where $S_n = C_n^{-1}$. By dropping the terms of $\mathcal{O}(\delta)$ and $\mathcal{O}(\varepsilon^2)$, we obtain the reconstruction formula

$$f^{(n)} \approx S_n[w_\delta^{(n)}(b) - w_0^{(n)}(b)]. \tag{44}$$

To obtain a stable reconstruction, we adopt the spectral cut-off regularization method. Since $|S_n| = |S_{-n}|$ for all $n \in \mathbb{N}$, the cut-off is symmetric with respect to $n = 0$ and the regularized reconstruction formula is given by

$$f(\theta) \approx \sum_{|n|\le N} f^{(n)} e^{\mathrm{i}n\theta}, \tag{45}$$

where $N \in \mathbb{N}$ is an empirical cut-off frequency and may be determined based on the discrepancy principle if the noise level δ is known.

The reconstruction method is simple and efficient: apply the fast Fourier transform (FFT) on the data $w_\delta(b)$ to obtain $w_\delta^{(n)}(b)$, substitute into (44) to find $f^{(n)}$, and insert into (45) to retrieve the deformation function f.

In [4, 12], the scaling factor S_n may have much more explicit forms. For example, in the perfectly electrical conducting diffraction grating problem, it is given by

$$S_n(h) = -\frac{\mathrm{i}}{2\kappa} e^{-\mathrm{i}\beta_n h},$$

where

$$\beta_n = \begin{cases} \sqrt{\kappa^2 - n^2}, & |n| < \kappa, \\ \mathrm{i}\sqrt{n^2 - \kappa^2}, & |n| > \kappa. \end{cases}$$

It is clear to note that $|S_n|$ is a constant for $|n| < \kappa$ and increases exponentially for $|n| > \kappa$. The transition occurs precisely at $|n| = \kappa$, which corresponds to the critical frequency for achieving subwavelength resolution. The inverse problem is severely ill-posed. Moreover, $|S_n(h)|$ also increases exponentially with respect to h. Thus the reconstruction deteriorates quickly as h increases, which implies the data must be measured at a very small distance from the surface in order to achieve subwavelength resolution.

Remark 5. The notion of "subwavelength" can be defined precisely when the scatterer is a small perturbation of a plane. For a Λ-periodic infinite surface $f(x)$, a frequency mode $f_n e^{\mathrm{i}\alpha_n x}$ belongs to the subwavelength regime if $n > \Lambda/\lambda$ since the space between two crests is $\Delta x = \Lambda/n < \lambda$. In our case we may define that the frequency mode $f_n e^{\mathrm{i}n\theta}$ belongs to the subwavelength regime if $n > 2\pi a/\lambda$ since the distance between two crests is

$$\Delta r \approx \frac{2\pi a}{n} < \lambda.$$

Hence the role of the period Λ in the diffraction grating problem is nearly equivalent to the role of the perimeter $2\pi a$ in the obstacle problem.

A precise behavior is not immediately seen for our S_n due to its complex form. In particular, it is not clear whether C_n is never zero so that S_n is always well defined. The following theorem shows that it is true, at least when h is sufficiently small.

Theorem 4.1. *For fixed n, it holds*

$$C_n(h) = C + \mathcal{O}(h) \quad \text{as } h \to 0, \tag{46}$$

where C is a nonzero constant independent of h and n.

Proof. For simplicity of notations, we drop the hats over all the variables in the proof. By (30) and the Wronskian formula for the Hankel functions, we have

$$E_n(a) = 0, \quad E_n'(a) = -\frac{4\mathrm{i}}{\pi a H_n^{(1)}(a)}. \tag{47}$$

Substituting them into (36)–(38) and using the Taylor series expansion yield

$$M_1 = \frac{Ch}{H_n^{(1)}(a)} + \mathcal{O}(h^2), \quad M_2 = \mathcal{O}(h^2), \quad M_3 = \mathcal{O}(h^3), \tag{48}$$

where C is a nonzero constant independent of h and n. Using the Taylor series expansion again for $H_n^{(1)}(s)$ yields

$$\frac{H_n^{(1)}(b)}{H_n^{(1)}(a)} = 1 + \mathcal{O}(h). \tag{49}$$

Substituting (48) and (49) into (35) yields the desired result (46). □

We may also compute the value of S_n numerically and investigate its dependence on the parameters κ, n, a, and h. Since the problem is invariant under the scaling of the wavelength, we fix $\kappa = 2\pi$, which corresponds to a wavelength $\lambda = 1$. First we investigate the dependence on n for fixed a and h. Consider an obstacle with base radius $a = \lambda$ and measurement distance $h = 0.1\lambda, 0.2\lambda, 0.3\lambda$, respectively. In Figure 2(a) the magnitude of S_n is plotted against $n \in [0, 50]$. Clearly the dependence of $|S_n|$ on n is similar as that in the infinite surface problems, i.e. its value remains small and relatively constant for smaller n and and grows exponentially for larger n. The transition occurs approximately at $n = 2\pi a/\lambda$, which corresponds to the critical frequency for subwavelength resolution in view of Remark 5. Hence it is stable to reconstruct rough features in the resonance (wavelength comparable) region and exponentially more unstable to reconstruct finer features in the subwavelength region. Moreover, the growth rate is roughly proportional to h, which means the reconstruction is more stable when the data is measured at a closer distance from the obstacle. This is in accordance with the physical principle of near-field imaging since the evanescent wave decays exponentially away from the object.

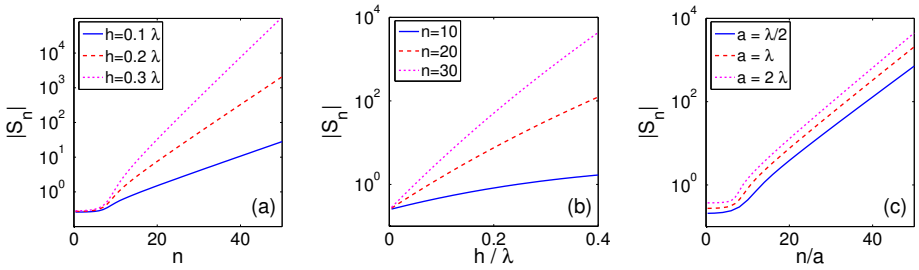

FIGURE 2. Dependence of $|S_n|$ on parameters n, h, a.

Next we investigate the dependence on the measurement distance h. Let $a = \lambda$ be fixed. In Figure 2(b) the magnitude of S_n is plotted against $h \in [0, 0.4\lambda]$ for $n = 10, 20, 30$ respectively. As anticipated we observe a nearly exponential growth of $|S_n|$ with respect to h and the growth rate is roughy proportional to n. Lastly we examine the effect of the base radius a. In view of Remark 5, we expect that the growth rate of $|S_n|$ is invariant in terms of n/a. This is confirmed in Figure 2(c), where $|S_n|$ is plotted against n/a for fixed $h = 0.2\lambda$ and $a = \lambda/2, \lambda, 2\lambda$ respectively. Hence the inverse problem has the same nature of ill-posedness regardless of the size of the obstacles.

Remark 6. The convergence of our method requires a dedicated regularity analysis of the solution for the direct scattering problem and is beyond the scope of this paper. We will study the convergence analysis in a future work. A related work can be found in [6] for the convergence analysis of the power series for solving a diffraction grating problem in near-field imaging.

4.2. **Nonlinear correction.** Due to the linearization error $\mathcal{O}(\varepsilon^2)$ in (43), the reconstruction deteriorates as the deformation parameter ε becomes larger. In this section we present a nonlinear correction scheme that can improve the results.

Rewrite (43) as

$$f^{(n)} = S_n[w_\delta^{(n)}(b) - w_0^{(n)}(b) + \rho], \tag{50}$$

where ρ is denoted as the remainder. Given the measurement data $w_\delta(b,\theta)$ or its Fourier coefficient $w_\delta^{(n)}(b)$, an approximation $\check{f}$ can be obtained by using (44). Based on $\check{f}$, we may solve the direct problem and obtain the computed data $\check{w}^{(n)}(b)$. Applying (50) on $\check{f}$ yields

$$\check{f}^{(n)} = S_n[\check{w}^{(n)}(b) - w_0^{(n)}(b) + \check{\rho}], \tag{51}$$

where $\check{\rho}$ is the remainder for the approximate solution. Subtracting (51) from (50) yields the correction term

$$f^{(n)} - \check{f}^{(n)} = S_n[w_\delta^{(n)}(b) - \check{w}^{(n)}(b) + \rho - \check{\rho}].$$

Dropping $\rho - \check{\rho}$, we obtain the updated Fourier coefficients

$$f^{(n)} \approx \check{f}^{(n)} + S_n[w^{(n)}(b) - \check{w}^{(n)}(b)].$$

The above discussion leads to an iterative scheme formulated in Algorithm 1.

Initialize: Set $k = 0$. Given the data $w_\delta(b,\theta)$, compute its Fourier coefficient $w_\delta^{(n)}(b)$ by using the FFT; compute the Fourier coefficients

$$f_0^{(n)} = S_n\left[w_\delta^{(n)}(b) - w_0^{(n)}\right].$$

Generate an initial approximation by using the inverse FFT:

$$f_0(\theta) = \sum_{|n|\le N} f_0^{(n)} e^{in\theta}.$$

while *stopping criterion is not met* **do**

Based on f_k, solve the direct problem to obtain $\check{w}_k(b)$ and its Fourier coefficient $\check{w}_k^{(n)}(b)$, update the Fourier coefficients

$$f_{k+1}^{(n)} = f_k^{(n)} + S_n[w_\delta^{(n)}(b) - \check{w}_k^{(n)}(b)].$$

Generate a new approximation f_{k+1}:

$$f_{k+1}(\theta) = \sum_{|n|\le N} f_{k+1}^{(n)} e^{in\theta}.$$

$k \leftarrow k+1$.

end

Algorithm 1: Reconstruction with a nonlinear correction.

5. **Numerical results.** In this section we present several numerical experiments to demonstrate the effectiveness of our method, examine the dependence of the results on h and ε, and show the improved results by using the nonlinear correction.

To avoid the so-called "inverse crime", we simulate the scattering data by solving the direct problem with an integral equation method in Theorem A.3 instead of the method of transformed field expansion in [30]. We add noise to the exact data:

$$w_\delta(b,\theta) = w(b,\theta)[1 + \delta\,\mathrm{rand}],$$

where rand denotes a uniformly distributed random number in $[-1,1]$. The wavenumber is $\kappa = 2\pi$, which corresponds the wavelength $\lambda = 1$ and ensures that all physical lengths are normalized with respect to the wavelength.

5.1. **Example 1.** Consider an obstacle with base radius $a = \lambda$. The exact deformation function is given by $f(\theta) = \varepsilon g(\theta)$ where

$$g(\theta) = 0.5\sin(4\theta) + 0.5\sin(16\theta).$$

In Remark 5, the Fourier modes f_n belongs to the subwavelength regime if $n > 2\pi a/\lambda = 2\pi$. Hence this particular deformation function contains both resonance and subwavelength features. First we examine the dependence of the reconstruction on the deformation parameter ε. Let $h = 0.1\lambda$ and $\delta = 0.05$ be fixed. In Figure 3(a) and 3(b), the exact $g(\theta)$ (solid line) is plotted against the reconstructed one (dashed line) for $\varepsilon = 0.01$ and $\varepsilon = 0.08$ respectively. We observe that subwavelength resolution is achieved in both cases. Clearly better result is obtained for smaller ε. All the fine features are completely resolved when $\varepsilon = 0.01$, while some amplitude information is lost when $\varepsilon = 0.08$.

Next we investigate the dependence of the reconstruction on the measurement distance h. Let $\varepsilon = 0.01$ and $\delta = 0.05$ be fixed. The results for $h = 0.1\lambda$ and $h = 0.2\lambda$ are show in Figure 3 (a) and (c) respectively. Apparently the reconstruction becomes unstable and the result deteriorates as h increases. Hence one should measure as close as possible to the obstacle to achieve higher resolutions. Finally we consider the effect of the noise level δ. Figure 3 (d) shows the result where the values of ε and h are the same as used in Figure 3 (c) but the δ is decreased from 0.05 to 0.01. As expected, a better reconstruction is achieved with a lower noise level.

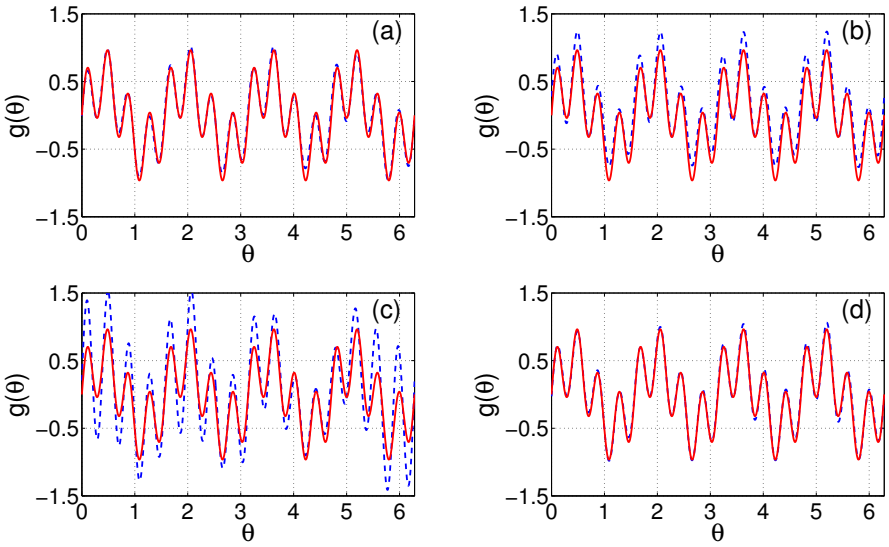

FIGURE 3. Example 1: A model problem with $a = \lambda$. The exact surface profile (normalized, solid line) is plotted against the reconstructed profile (normalized, dashed line) using different values of ε, h and δ. (a) $\varepsilon = 0.01, h = 0.1\lambda, \delta = 0.05$; (b) $\varepsilon = 0.08, h = 0.1\lambda, \delta = 0.05$; (c) $\varepsilon = 0.01, h = 0.2\lambda, \delta = 0.05$; (d) $\varepsilon = 0.01, h = 0.2, \delta = 0.01$.

The measurement distance h and noise level δ may be made small through better facilities. The error due to deformation parameter ε is induced by the linearization

and is intrinsic to the mathematical model. For small ε, the results are already satisfactory and no correction is needed. However, the nonlinear correction is necessary in order to obtain good reconstruction for larger ε. Now we test the proposed Algorithm 1 and show the improvement that can be made in the reconstruction. Let $\varepsilon = 0.1, h = 0.2\lambda, \delta = 0.01$ be fixed. Figure 4(a) shows the original result without nonlinear correction. As before some amplitude information is not completely reconstructed. Figure 4(b) shows the result after 10 iterations of the correction algorithm. We observe a dramatic improvement, where the lost amplitude information is completely retrieved and the result is as good as the one shown in Figure 3(d) where $\varepsilon = 0.01$ is much smaller. Figure 4(c) shows the convergence plot of the relative L^2 error.

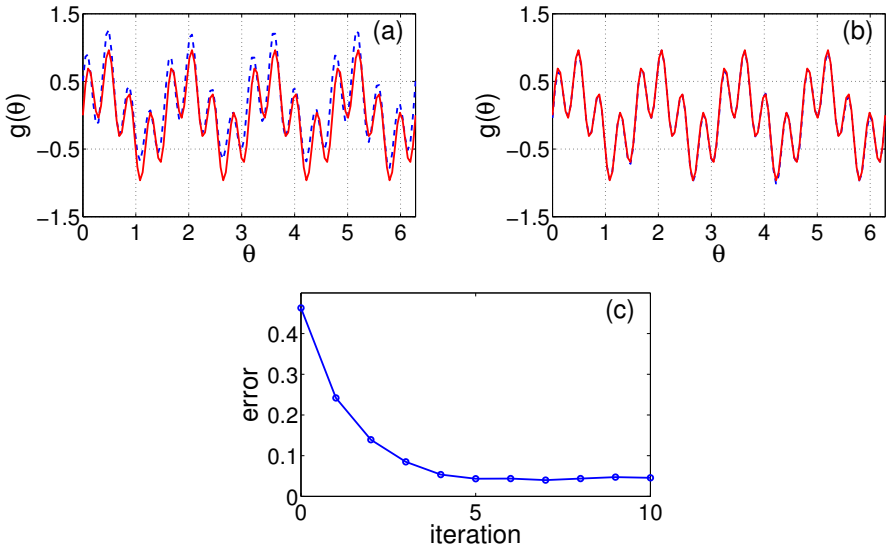

FIGURE 4. Example 1: A model problem with $a = \lambda$. The exact surface profile (normalized, solid line) is plotted against the reconstructed profile (normalized, dashed line). The parameters $\varepsilon = 0.1, h = 0.2\lambda, \delta = 0.01$ are fixed. (a) without nonlinear correction; (b) after 10 iterations of nonlinear correction; (c) convergence plot of the relative L^2 error.

5.2. **Example 2.** Now we consider a smaller obstacle where the base radius $a = \lambda/(2\pi)$. Thus the Fourier modes f_n belongs to the subwavelength regime if $n > 1$. Let the normalized deformation function be given by

$$g(\theta) = 0.5\sin(\theta) + 0.5\sin(4\theta).$$

The observations on the dependence of the reconstructions on the parameters are similar as those in the first example, so we only show the results for different ε and the nonlinear correction. Since ε is not too small relative to a in this example, we are able to draw the results in polar coordinate and essential features are visible. Let $h = 0.1\lambda$ and $\delta = 0.05$ be fixed. In Figure 5(a), 5(b), 5(c), the exact obstacles (solid line) are plotted against the reconstructed obstacles (dashed line) for $\varepsilon = 0.02, 0.04, 0.08$ respectively. Figure 5 shows the result with $\varepsilon = 0.08$ after

10 iterations of nonlinear correction. Since the perimeter of the base disk is λ, any perturbation on the obstacle is beyond diffraction limit. Hence we also obtained subwavelength resolution in all cases. The best result is achieved with smallest ε and nonlinear correction can improve the results dramatically.

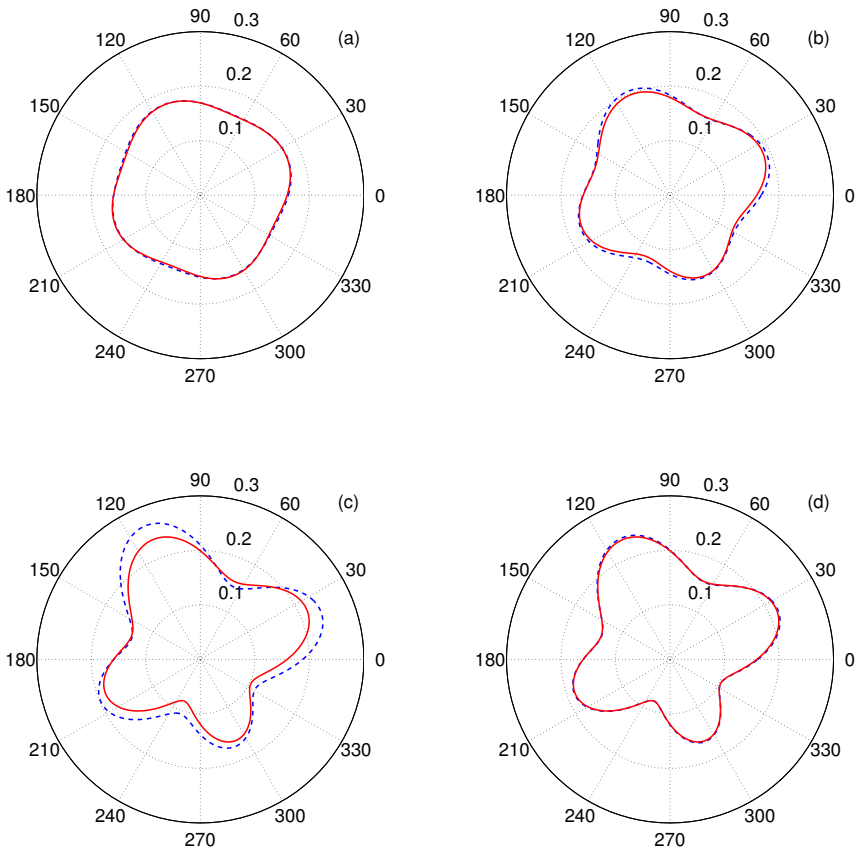

FIGURE 5. Example 2: A model problem with $a = \lambda/2\pi$. The parameters $h = 0.1\lambda$ and $\delta = 0.05$ are fixed. The exact obstacle (solid line) is plotted against the reconstructed obstacle (dashed line). (a) $\varepsilon = 0.02$; (b) $\varepsilon = 0.04$; (c) $\varepsilon = 0.08$; (d) $\varepsilon = 0.08$, after 10 iterations of nonlinear correction is applied.

6. **Conclusion.** We presented a numerical method for near-field imaging of sound soft obstacles in two dimensions. The surface was assumed to be a small and smooth deformation of a circle. Based on the transformed field expansion, we converted the original BVP into a successive sequence of BVPs in an annulus and derived their analytic solutions. Dropping higher order terms in the power series expansion, we linearized the nonlinear inverse problem and obtained an explicit reconstruction formula. A nonlinear correction scheme was devised to improve the results for large deformation. The method requires only a single cylindrical incident wave at a fixed

frequency. Numerical tests showed that the method is effective and efficient to achieve subwavelength resolution. Better resolution was obtained by using smaller parameters, which is in accordance with the principle of near-field imaging.

Although the method is derived for sound soft obstacles, similar reconstruction formulas are expected for sound hard and impedance boundary conditions. It is also worthwhile to consider the transmission problem in which the obstacle is penetrable. We chose cylindrical incident wave because of its mathematical simplicity. We will consider the commonly used plane wave as the incident field in a future work. Other interesting and challenging problems include inverse scattering with limited aperture and/or phaseless data. Finally we wish to extend the proposed method to three-dimensional obstacles, where the full Maxwell equations should be considered.

Appendix A. **Direct problem.** Due to the singularity of the incident wave, the usual boundary integral equations for plane incident wave [14] need to be modified. We derive new equations to accommodate the change in this section.

Let Ω be a bounded domain in $\mathbb{R}^2$, which contains the origin and has a C^2 boundary $\partial\Omega$. Consider the incident field

$$u^{\text{inc}}(x) = H_0^{(2)}(\kappa|x|),$$

where $x = (x_1, x_2) \in \mathbb{R}^2$ and κ is the wavenumber. Let $u^{\text{sca}}(x)$ be the scattered field satisfying the Sommerfeld radiation condition

$$\lim_{|x|\to\infty} \sqrt{|x|}\left(\partial_{|x|} - \mathrm{i}\kappa\right) u^{\text{sca}}(x) = 0 \tag{A.1}$$

uniformly for all directions $x/|x|$. The fundamental solution for the Helmholtz equation in $\mathbb{R}^2$ is given by

$$G(x,y) = \frac{\mathrm{i}}{4} H_0^{(1)}(\kappa|x-y|), \tag{A.2}$$

where $y = (y_1, y_2) \in \mathbb{R}^2$.

Lemma A.1. *The incident field u^{inc} satisfies*

$$\int_{\partial\Omega} u^{\text{inc}}(y)\partial_{n_y} G(x,y) - G(x,y)\partial_{n_y} u^{\text{inc}}(y)\mathrm{d}s(y) = \begin{cases} -2J_0(\kappa|x|), & x \in \Omega, \\ -H_0^{(1)}(\kappa|x|), & x \in \mathbb{R}^2 \setminus \bar{\Omega}, \end{cases} \tag{A.3}$$

where J_0 is the zeroth order Bessel function of the first kind.

Proof. Let $x \in \Omega$ be fixed. First assume $x \neq 0$. Then $G(\cdot, y)$ has a singularity at $y = x$ and $u^{\text{inc}}(y)$ has a singularity at $y = 0$, both of which are inside Ω. Let $B(x,\sigma)$ and $B(0,\tau)$ be balls centered at $x, 0$ with radius σ, τ respectively, where σ, τ are sufficiently small so that $B(x,\sigma), B(0,\rho) \subset \Omega$ and $B(x,\sigma) \cap B(0,\rho) = \emptyset$. See Figure 6 for a depiction. Applying the second Green's identity and using the Helmholtz equations for $G(\cdot, y)$ and $u(y)$ in the domain $\Omega \setminus (B(x,\sigma) \cup B(0,\tau)$, we obtain

$$\begin{aligned} &\int_{\partial\Omega\cup\partial B(x,\sigma)\cup\partial B(0,\tau)} \left[u^{\text{inc}}(y)\partial_{n_y} G(x,y) - G(x,y)\partial_{n_y} u^{\text{inc}}(y)\right] \mathrm{d}s(y) \\ &= \int_{\Omega\setminus[B(x,\sigma)\cup B(0,\tau)]} \left[u^{\text{inc}}(y)\Delta G(x,y) - G(x,y)\Delta u(y)\right] \mathrm{d}y \end{aligned}$$

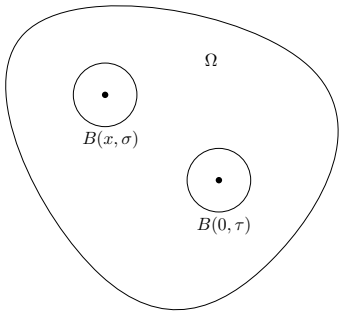

FIGURE 6. Illustration for the proof of Lemma A.1.

$$= \int_{\Omega\setminus[B(x,\sigma)\cup B(0,\tau)]} \left[-\kappa^2 u^{\text{inc}}(y)G(x,y) + \kappa^2 G(x,y)u(y)\right] \mathrm{d}y = 0. \tag{A.4}$$

Taking partial derivatives with respect to y on A.2 yields

$$\nabla_y G(x,y) = \frac{\mathrm{i}(y-x)}{4|y-x|}\left(H_0^{(1)}\right)'(\kappa|x-y|) = -\frac{\mathrm{i}(y-x)}{4|y-x|}H_1^{(1)}(\kappa|x-y|). \tag{A.5}$$

The normal vector n_y goes inward at $B(x,\sigma)$ and is given by

$$n_y = -\frac{y-x}{|y-x|}, \quad y \in \partial B(x,\sigma). \tag{A.6}$$

From (A.5) and (A.6) we obtain

$$\partial_{n_y} G(x,y) = \frac{\mathrm{i}\kappa}{4}H_1^{(1)}(\kappa|x-y|), \quad y \in \partial B(x,\sigma).$$

Using the asymptotic forms of Bessel functions for small arguments [22], we have

$$H_0^{(1)}(z) \sim \left(\frac{2\mathrm{i}}{\pi}\right)\ln z, \quad H_1^{(1)}(z) \sim \left(-\frac{2\mathrm{i}}{\pi}\right)z^{-1}, \quad \text{as } z \to 0,$$

which gives together with the mean value theorem that

$$\begin{aligned}
&\lim_{\sigma\to 0}\int_{\partial B(x,\sigma)} \left[u^{\text{inc}}(y)\partial_{n_y}G(x,y) - G(x,y)\partial_{n_y}u^{\text{inc}}(y)\right]\mathrm{d}s(y)\\
&= \lim_{\sigma\to 0}\frac{\mathrm{i}\kappa}{4}\int_{\partial B(x,\sigma)} \left[u^{\text{inc}}(y)H_1^{(1)}(\kappa|x-y|) - \partial_{n_y}u^{\text{inc}}(y)H_0^{(1)}(\kappa|x-y|)\right]\mathrm{d}s(y)\\
&= \lim_{\sigma\to 0}\frac{\mathrm{i}\kappa}{4}\int_{\partial B(x,\sigma)} \left[u^{\text{inc}}(y)H_1^{(1)}(\kappa\sigma) - \partial_{n_y}u^{\text{inc}}(y)H_0^{(1)}(\kappa\sigma)\right]\mathrm{d}s(y)\\
&= \frac{\mathrm{i}\kappa}{4}\left\{u^{\text{inc}}(x)\lim_{\sigma\to 0}\left[\left(-\frac{2\mathrm{i}}{\pi}\right)\frac{1}{\kappa\sigma}2\pi\sigma\right] - \partial_{n_x}u^{\text{inc}}(x)\lim_{\sigma\to 0}\left[\left(\frac{2\mathrm{i}}{\pi}\right)\ln(\kappa\sigma)2\pi\sigma\right]\right\}\\
&= u^{\text{inc}}(x) = H_0^{(2)}(\kappa|x|).
\end{aligned} \tag{A.7}$$

By similar calculations we obtain

$$\lim_{\tau\to 0}\int_{\partial B(0,\tau)} \left[u^{\text{inc}}(y)\partial_{n_y}G(x,y) - G(x,y)\partial_{n_y}u^{\text{inc}}(y)\right]\mathrm{d}s(y) = H_0^{(1)}(\kappa|x|). \tag{A.8}$$

Taking $\lim_{\sigma,\tau\to 0}$ on (A.4) and using (A.7), (A.8) yields

$$\begin{aligned}&\int_{\partial\Omega}\left[u^{\mathrm{inc}}(y)\partial_{n_y}G(x,y)-G(x,y)\partial_{n_y}u^{\mathrm{inc}}(y)\right]\mathrm{d}s(y)\\&=-\left[H_0^{(2)}(\kappa|x|)+H_0^{(1)}(\kappa|x|)\right]=-2J_0(\kappa|x|).\end{aligned}$$

Since both left and right hand side are continuous for $x\in\Omega$, the above identity is also valid when $x=0$, which completes the proof for the first part of (A.3). The proof for the second part is very similar and is omitted. □

By using the radiation condition (A.1) and similar arguments as in the proof of Lemma A.1, we can prove the following identity for the scattered field. The details may be found in [14] and are omitted here.

Lemma A.2. *The scattered field u^{sca} satisfies the relation:*

$$\begin{aligned}&\int_{\partial\Omega}\left[u^{\mathrm{sca}}(y)\partial_{n_y}G(x,y)-G(x,y)\partial_{n_y}u^{\mathrm{sca}}(y)\right]\mathrm{d}s(y)\\&=\begin{cases}0, & x\in D,\\ u^{\mathrm{sca}}(x), & x\in\mathbb{R}^2\setminus\bar{D}.\end{cases}\end{aligned}\tag{A.9}$$

The main result of this section follows from Lemma A.1 and A.2.

Theorem A.3. *Let $u=u^{\mathrm{inc}}+u^{\mathrm{sca}}$ be the total field and satisfies*

$$u(x)=0,\quad x\in\partial\Omega.\tag{A.10}$$

Then $\partial_n u$ satisfies

$$\begin{aligned}&\frac{1}{2}\partial_{n_x}u(x)+\int_{\partial\Omega}\left[\partial_{n_x}G(x,y)+\mathrm{i}\eta G(x,y)\right]\partial_{n_x}u(y)\mathrm{d}s(y)\\&=2(\partial_{n_x}+\mathrm{i}\eta)J_0(\kappa|x|),\quad x\in\partial\Omega,\end{aligned}\tag{A.11}$$

where $\eta\neq 0$ is a real coupling constant. The scattered field can be computed from

$$u^{\mathrm{sca}}(x)=H_0^{(1)}(\kappa|x|)-\int_{\partial\Omega}G(x,y)\partial_{n_y}u(y)\mathrm{d}s(y),\quad x\in\mathbb{R}^2\setminus\bar{\Omega}.\tag{A.12}$$

Proof. Adding (A.3), (A.9) for $x\in\Omega$ and using the boundary condition (A.10), we obtain

$$\int_{\partial\Omega}G(x,y)\partial_{n_y}u(y)\mathrm{d}s(y)=2J_0(\kappa|x|),\quad x\in\Omega.$$

Taking $\partial_{n_x}+\mathrm{i}\eta$ on both sides and applying the well known jump conditions for the single and double layer potentials [14] yields (A.11). Equation (A.12) follows immediately from adding (A.3) and (A.9) for $x\in\mathbb{R}^2\setminus\bar{\Omega}$. □

Appendix B. **A two-point boundary value problem.** In this section we present a method to obtain analytical solutions for the BVP (25)–(27). The method is based on the solution for the following general boundary value problem:

$$Lu(x)=f(x),\quad x\in(a,b)\tag{B.1}$$

$$A_1u(a)+B_1u'(a)=0,\tag{B.2}$$

$$A_2u(b)+B_2u'(b)=0,\tag{B.3}$$

where L is the Sturm–Liouville operator given by

$$L = \frac{d}{dx}\left(p(x)\frac{d}{dx}\right) + q(x).$$

It is well known that the solution to the above BVP can be written as

$$u(x) = \int_a^b G(x,y)f(y)\mathrm{d}y,$$

where $G(x,y)$ is called the Green's function, which is unique and satisfies the following properties when considered as a function of x for fixed y:

1. satisfies the homogeneous Sturm–Liouville equation:
$$LG(x,y) = 0, \quad \text{in } (a,b)$$
for all $x \neq y$;
2. satisfies the homogeneous boundary conditions (B.2) and (B.3);
3. continuous for all x;
4. has continuous first and second derivatives for all $x \neq y$;
5. $\partial_x G(x,y)$ has a jump discontinuity at $x = y$ given by
$$\partial_x G(y^+,y) - \partial_x G(y^-,y) = \frac{1}{p(y)}.$$

It can be verified the unique Green's function satisfying the above properties is given by

$$G(x,y) = \frac{1}{C(y)}\begin{cases} u_1(x)u_2(y), & x < y, \\ u_1(y)u_2(x), & x > y, \end{cases} \tag{B.4}$$

where u_1, u_2 are linearly independent solutions to $Lu = 0$ with u_1 satisfying the boundary condition (B.2) and u_2 satisfying the boundary condition (B.3), and where

$$C(y) = p(y)\left[u_1(y)u_2'(y) - u_1'(y)u_2(y)\right]. \tag{B.5}$$

The BVP (25)–(27) can be written as the following Sturm–Liouville form:

$$Lu(x) = f(x), \quad x \in (a,b), \tag{B.6}$$

$$u(a) = \varphi, \tag{B.7}$$

$$u'(b) - \frac{\left(H_n^{(1)}\right)'(b)}{H_n^{(1)}(b)}u(b) = \psi, \tag{B.8}$$

where L is the Sturm-Liouville operator with

$$p(x) = x, \quad q(x) = x - \frac{n^2}{x}.$$

The solutions u_1 and u_2 in (B.5) are linearly independent solutions to the following problems:

$$\begin{aligned} Lu(x) &= 0, \quad x \in (a,b), \\ u(a) &= 0, \end{aligned}$$

and

$$Lu(x) = 0, \quad x \in (a,b),$$

$$u'(b) - \frac{\left(H_n^{(1)}\right)'(b)}{H_n^{(1)}(b)} u(b) = 0.$$

Since L is the Bessel operator of order n, a set of linearly independent solutions u_1 and u_2 are given by

$$u_1 = E_n(x), \quad u_2 = H_n^{(1)}(x),$$

where E_n is defined in (30). Substituting the above solutions into (B.5) yields

$$C(y) = \frac{4\mathrm{i}}{\pi},$$

By (B.4) we obtain the Green's function

$$G(x,y) = \frac{\pi}{4\mathrm{i}} \begin{cases} E_n(x) H_n^{(1)}(y), & x < y, \\ E_n(y) H_n^{(1)}(x), & x > y. \end{cases}$$

After the Green's function $G(x,y)$ is found, the solution to the BVP (B.6)–(B.8) can be written as

$$u(x) = c_1 H_n^{(1)}(x) + c_2 H_n^{(2)}(x) + \int_a^b G(x,y) f(y) \mathrm{d}y.$$

Applying the boundary conditions (B.7) and (B.8) yields

$$u(x) = \frac{H_n^{(1)}(x)}{H_n^{(1)}(a)} \varphi - G(x,b) b \psi + \int_a^b G(x,y) f(y) \mathrm{d}y. \tag{B.9}$$

REFERENCES

[1] G. Bao, T. Cui and P. Li, Inverse diffraction grating of Maxwell's equations in biperiodic structures, *Optics Express,* **22** (2014), 4799–4816.

[2] G. Bao and P. Li, Inverse medium scattering problems in near-field optics, *J. Comput. Math.,* **25** (2007), 252–265.

[3] G. Bao and P. Li, Numerical solution of inverse scattering for near-field optics, *Optics Lett.,* **32** (2007), 1465–1467.

[4] G. Bao and P. Li, Near-field imaging of infinite rough surfaces, *SIAM J. Appl. Math.,* **73** (2013), 2162–2187.

[5] G. Bao and P. Li, Near-field imaging of infinite rough surfaces in dielectric media, *SIAM J. Imaging Sci.,* **7** (2014), 867–899.

[6] G. Bao and P. Li, Convergence analysis in near-field imaging, *Inverse Problems,* **30** (2014), 085008, 26PP.

[7] G. Bao and J. Lin, Imaging of reflective surfaces by near-field optics, *Optics Lett.,* **37** (2012), 5027–5029.

[8] G. Bao and J. Lin, Near-field imaging of the surface displacement on an infinite ground plane, *Inverse Probl. Imag.,* **7** (2013), 377–396.

[9] O. Bruno and F. Reitich, Numerical solution of diffraction problems: A method of variation of boundaries, *J. Opt. Soc. Am. A,* **10** (1993), 1168–1175.

[10] F. Cakoni and D. Colton, *Qualitative Methods in Inverse Scattering Theory: An Introduction,* Springer, Berlin, 2006.

[11] P. Carney and J. Schotland, Near-field tomography, in *Inside Out: Inverse Problems and Applications* (ed. G. Uhlmann), Cambridge University Press, **47** (2003), 133–168.

[12] T. Cheng, P. Li and Y. Wang, Near-field imaging of perfectly conducting grating surfaces, *J. Opt. Soc. Am. A,* **30** (2013), 2473–2481.

[13] D. Colton and A. Kirsch, A simple method for solving inverse scattering problems in the resonance region, *Inverse Problems,* **12** (1996), 383–393.

[14] D. Colton and R. Kress, *Integral Equation Methods in Scattering Theory*, Wiley, New York, 1983.

[15] D. Colton and R. Kress, *Inverse Acoustic and Electromagnetic Scattering Theory*, Springer-Verlag, Berlin, 1998.
[16] D. Courjon, *Near-field Microscopy and Near-field Optics*, Imperial College Press, London, 2003.
[17] D. Courjon and C. Bainier, Near field microscopy and near field optics, *Rep. Prog. Phys.,* **57** (1994), 989–1028.
[18] F. Hettlich, Frechét derivatives in inverse obstacle scattering, *Inverse Problems,* **11** (1995), 371–382.
[19] M. Ikehata, Reconstruction of an obstacle from the scattering amplitude at a fixed frequency, *Inverse Problems,* textbf14 (1998), 949–954.
[20] A. Kirsch, The domain derivative and two applications in inverse scattering theory, *Inverse Problems,* **9** (1993), 81–96.
[21] A. Kirsch, The music algorithm and the factorization method in inverse scattering theory for inhomogeneous media, *Inverse Problems,* **18** (2002), 1025–1040.
[22] NIST Digital Library of Mathematical Functions. `http://dlmf.nist.gov/`, Release 1.0.6 of 2013-05-06.
[23] R. Kress, Newton's method for inverse obstacle scattering meets the method of least squares, *Inverse Problems,* **19** (2003), S91–S104.
[24] R. Kress and W. Rundell, A quasi-Newton method in inverse obstacle scattering, *Inverse Problems,* **10** (1994), 1145–1157.
[25] P. Li and J. Shen, Analysis of the scattering by an unbounded rough surface, *Math. Meth. Appl. Sci.,* **35** (2012), 2166–2184.
[26] A. Malcolm and D. P. Nicholls, A field expansions method for scattering by periodic multi-layered media, *J. Acout. Soc. Am.,* **129** (2011), 1783–1793.
[27] A. Malcolm and D. P. Nicholls, A boundary perturbation method for recovering interface shapes in layered media, *Inverse Problems,* **27** (2011), 095009, 18pp.
[28] D. P. Nicholls and F. Reitich, Shape deformations in rough surface scattering: Cancellations, conditioning, and convergence, *J. Opt. Soc. Am. A,* **21** (2004), 590–605.
[29] D. P. Nicholls and F. Reitich, Shape deformations in rough surface scattering: improved algorithms, *J. Opt. Soc. Am. A,* **21** (2004), 606–621.
[30] D. P. Nicholls and J. Shen, A Stable High-Order Method for Two-Dimensional Bounded-Obstacle Scattering, *SIAM J. Sci. Comput.,* **28** (2006), 1398–1419.
[31] R. Potthast, Stability estimates and reconstructions in inverse acoustic scattering using singular sources, *J. Comp. Appl. Math.,* **114** (2000), 247–274.
[32] R. Schmidt, Multiple emitter location and signal parameter estimation, *IEEE Trans. Antennas Propag.,* **34** (1986), 276–280.

Received January 2014; revised June 2014.

E-mail address: lipeijun@math.purdue.edu
E-mail address: wang2049@math.purdue.edu